Sensing and Bio-Sensing Research 44 (2024) 100656

Contents lists available at ScienceDirect

Sensing and Bio-Sensing Research

journal homepage: www.elsevier.com/locate/sbsr

Light-sheet skew rays sensing platform based on microstructuring of coreless multimode fiber

Lukui Xu [a,b], Tingting Zhuang [a,b], Bonan Liu [a,b], Jinyu Wang [c], Mamoona Khalid [d], Soroush Shahnia [e], Christophe A. Codemard [f], Zhiyong Bai [a,b], Shen Liu [a,b], Ying Wang [a,b], George Y. Chen [a,b,*], Yiping Wang [a,b]

[a] Key Laboratory of Optoelectronic Devices and Systems of Ministry of Education and Guangdong Province, College of Physics and Optoelectronic Engineering, Shenzhen University, Shenzhen 518060, China

[b] Shenzhen Key Laboratory of Photonic Devices and Sensing Systems for Internet of Things, Guangdong and Hong Kong Joint Research Centre for Optical Fiber Sensors, Shenzhen University, 518060 Shenzhen, China

[c] Key Laboratory of Optical Fiber Technology of Shandong Province; Qilu University of Technology (Shandong Academy of Sciences), Laser Institute, Jinan, Shandong 250014, China

[d] Photonics and Communications lab, Electrical Engineering Department, University of Engineering and Technology, 47050 Taxila, Pakistan

[e] Laser Physics and Photonic Devices Laboratories, School of Engineering, University of South Australia, Mawson Lakes, South Australia 5095, Australia

[f] TRUMPF Advanced Laser Laboratory, University of Southampton, Southampton SO17 1BJ, United Kingdom

ARTICLE INFO

Keywords:
Light sheet
Skew rays
Multimode fiber
Chemical sensor
Rhodamine B
Fiber-optic sensor

ABSTRACT

Given the increasing demands for quality assurance in the food industry, a significant challenge emerges in the form of expensive integration of food sensors into packaging. This integration is crucial for strengthening food safety measures and ensuring the impeccable quality of food products. Official laboratory food safety testing heavily relies on expensive and bulky equipment. This article presents a new chemical sensing platform and a comparative study of in-house built novel designs for a robust multimode chemical sensor head probed by highly sensitive light-sheet skew rays for addressing cost and footprint issues. The sensing mechanism is the interaction between evanescent field mediated by refined skew rays propagating through a structured coreless multimode fiber and external chemicals, resulting in probe light absorption. The sensitivity is enhanced by the controlled excitation of skew rays using a light sheet and four specially engineered coreless multimode fiber structure, including uniform, tapered, microstub and microbubble designs. The sensitivity was demonstrated to be as high as 0.046 (dB/cm) / $dB_{(1\ ng/ml)}$ and the limit of detection as low as 1.028 ng/ml for the microbubble structure. The results of our research pave the groundwork for a new range of chemical sensors suitable for food safety monitoring.

1. Introduction

Consuming contaminated food, containing harmful fungi (such as FB1), bacteria, viruses, parasites or chemicals, can lead to over 200 types of diseases ranging from diarrhea to cancer. It is estimated that globally, 600 million people fall ill and 420,000 die each year due to foodborne illnesses.[1] Lower-middle-income countries suffer a loss of $110 billion annually in productivity and healthcare costs due to unsafe food.[1] Therefore, better monitoring of food can reduce the occurrence and severity of foodborne illnesses, thus protecting public health. Food packaging generates billions of dollars in daily sales worldwide. However, inserting sensors for detecting toxins within food packaging requires substantial investment.[2] Currently, official laboratory-based food safety testing heavily relies on expensive and bulky equipment, such as liquid/gas chromatography and mass spectrometry, to gather data for evaluating degradation processes and establishing models to estimate expiration dates. However, these methods are limited by the need for trained personnel to handle sampling and sample transfer, thus constraining their practical application.

Researchers have investigated the use of multimode fibers in

* Corresponding author at: Key Laboratory of Optoelectronic Devices and Systems of Ministry of Education and Guangdong Province, College of Physics and Optoelectronic Engineering, Shenzhen University, Shenzhen 518060, China.

E-mail address: gychen@szu.edu.cn (G.Y. Chen).

https://doi.org/10.1016/j.sbsr.2024.100656
Received 11 November 2023; Received in revised form 7 May 2024; Accepted 20 May 2024
Available online 23 May 2024

chemical sensors that operate on the principle of evanescent waves.[3–14] This approach provides advantages such as durability, widespread availability in the market, and affordability. Pump light or spectral absorption has been widely employed as a sensing mechanism for detecting and quantifying biological or chemical concentration in various fields such as healthcare, manufacturing and security.[15–21] To enhance sensitivity and detection limits/accuracy, stronger pump light absorption is desirable. However, highly sensitive probes are well known to be fragile, such as nanofiber tapers. For this purpose, researchers have utilized focused rays or skew rays to excite higher order modes in robust multimode fibers, thereby enhancing the interaction between light and substances[22–27] while ensuring a reasonable sensor lifespan.

Ruoyu Wang et al.[22] developed a novel evanescent-wave all-fiber biosensor (EWA) employing aptamer-modified magnetic beads combined with STV-coupled DNA probes, and desulfurized biotin-modified fibers to achieve highly sensitive detection of ochratoxin A (OTA). This strategy demonstrates excellent reusability and high sensitivity through target-triggered signaling probe release and specific recognition in the EWA system, reinforcing the potential application of aptamer sensors for multi-toxicity analyte detection. J. Ma et al.[24] developed a non-Lambertian fiber-optic side-emitting diffuser (FOSED), which was experimentally verified to significantly improve signal quality and reduce stray light, optimize excitation power utilization, and reduce the system's dependence on light source power and filter performance. Compared with long-period grating sensors, FOSED demonstrates a more efficient mode coupling capability, providing a new idea for high-performance and low-cost electronic warfare sensor design.

In this study, four different innovative coreless multimode fiber structures were developed to optimize the interaction between light and target substances for chemical sensing. These structures were designed to amplify the evanescent field by employing the Light-Sheet Skew Ray (LSSR) excitation approach.[25] Rhodamine B was used as benchmark test chemical to demonstrate the effectiveness of these structures. For the four sensing structures, the skew rays undergo total internal reflection with the external environment as the cladding, and thus the evanescent field of light interacts with the analyte surrounding the fiber. As such, the concentration affects the attenuation. This means the higher the concentration, the stronger the light absorption or attenuation. The sensing platform consisted of a beam shaper to generate a light sheet for exciting a controlled group of skew rays in a low-index-coated coreless multimode fiber. Skew rays increase the total number of total internal reflections relative to meridional rays, and thus achieves higher sensitivity and facilitates a more uniform integration region. The sensing region is reengineered based on the selected sensing structure to increase evanescent field overlap with the external environment, further enhancing the sensitivity. Overall, the new method features robustness and high sensitivity, and can potentially be manufactured at a low cost with a fixed-angle configuration.

2. Materials and methods

2.1. Materials

In this study, Rhodamine B was selected as the target chemical due to its light absorption characteristics at a laser wavelength of 532 nm. To prepare the solution, 1 mg of Rhodamine B powder was accurately measured using a precision balance, Subsequently, 10 ml of deionized water was added to the powder, resulting in the creation of a 10 ml Rhodamine B solution featuring a concentration of 100 μg/ml. Next, 1 ml of this solution was diluted with 9 ml of deionized water to obtain a Rhodamine B solution with a concentration of 10 μg/ml. This stepwise dilution procedure was iterated to achieve a series of Rhodamine B solutions characterized by concentrations of 1 ng/ml, 100 ng/ml, 10 ng/ml, 1000 ng/ml, 10,000 ng/ml, respectively. In addition, a coreless multimode fiber was used as the sensing fiber, Rhodamine B from SIGMA(R4127), light source from Thorlabs (DJ532–10) and power meter from Newport (918D-IS-1, 1936-R).

2.2. Methodology

The propagation characteristics of higher-order modes in an optical fiber's evanescent field exhibit a distinctive attribute that extends beyond the core-cladding interface. This extension augments the penetration depth of light into the surrounding medium and intensifies the interaction with substances located on the fiber's surface. As a result, there emerges an increased sensitivity conducive to evanescent wave-based sensors.[5–13,22,28] In certain cases, these skew rays are referred to as leaking rays or tunneling rays as they do not intersect with the waveguide axis.[29]

A specific degree of skewness can be induced along the meridional axis by reflecting the meridional rays from a curved waveguide interface.[30] The skew rays can be generated by launching light from one end of the fiber at an angle non-parallel to the axis of the waveguide's cross-sectional area responsible for meridional axis generation. These skew rays can be characterized mathematically employing two angular parameters, described in relation to the longitudinal and transverse orientations with respect to the outer interface of the waveguide shown in Fig. 1.

Skew rays have the capacity to induce a greater occurrence of total internal reflection (N_r) when considering a consistent emission angle (θ) in comparison to their meridional counterparts, as shown in eq. (1).[31] This phenomenon holds the potential to enhance the sensitivity of numerous sensing mechanisms, including but not limited to optical confinement absorption, molecular absorption (such as pump light absorption), and fluorescence excitation.

$$N_r = 1/\left[\left(\frac{2R\cos\theta_{\varnothing}}{\cos\theta_z} + d\right)\cdot\sin\theta_z\right] \tag{1}$$

where R is the core radius (i.e., the cladding is a functional coating); d is

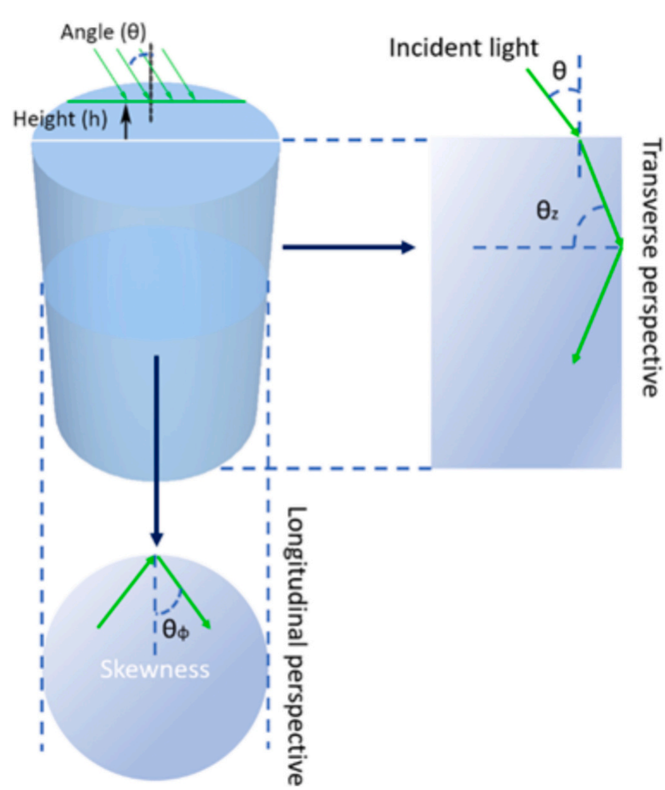

Fig. 1. Concept of light-sheet excited skew rays.

the penetration length of each reflection (i.e., Goos-Hänchen shift); $\theta_z = \frac{\pi}{2} - sin^{-1}\left(\frac{sin\theta}{n}\right)$ is the angle between the ray and the normal of the core-cladding interface seen from the transverse perspective; $\theta_{\varnothing} = \frac{\pi}{2} - cos^{-1}\left(\frac{i}{N}\right)$ is the angle between the ray and the normal of the core-cladding interface seen from the longitudinal perspective, which represents skewness; N_r is the refractive index of the optical fiber; i represents the integer step offset from the center of the optical fiber; N represents the total number of steps from the center of the fiber to the edge. Skew rays can also be excited at larger θ, far exceeding the upper limit of the meridional rays. In contrast to the optical phase interference measurement techniques, optical power-based measurement mechanisms are less sensitive to temperature. In other words, power-based sensing mechanisms exhibit a smaller response to temperature variations.[32]

A series of scans were conducted to establish the correlation between the quantified value, specifically the concentration of dye and the detection parameter (attenuation) to facilitate subsequent determinations of dye concentration. These scans involved altering the parameters θ and core offset at each incremental concentration level. Simultaneously, the residual pump power was gauged to facilitate the computation of the corresponding attenuation value. The residual pump power is monitored instead of fluorescence intensity or Raman scattered signal to achieve a higher signal-to-noise ratio, at the expense of non-specificity. To avoid the unwanted contribution of ambient light in the experiments, the experiment setup was shielded and the power meter was zeroed before each experiment. In addition, the experiment setup was conducted on an air-suspended optical platform to minimize vibrations that may otherwise cause fluctuations in the input optical power.

2.3. Fabrication of sensing structures

One distinctive feature of this article is the design and characterization of sensing structures. Three different sensing structures are studied for absorption-based sensing: microbubble, microstub and tapered fiber. Due to the limited experimental conditions, the lengths of all sensing structures are not necessarily equal, and thus the sensitivity of each sensing structure is compared after length normalization. In addition to these structures, the pristine coreless multimode fiber, or uniform structure, is used as a control (as shown in Fig. 2).

The preparation of the uniform structure (Fig. 2a, Fig. 3) is relatively simple. The coating layer was stripped off for a length of 3 cm at the position of the fiber used for sensing. The exposed 3 cm length of cladding was then wiped with anhydrous ethanol to remove debris, allowing for full contact between the exposed cladding and the Rhodamine B solution. When total internal reflection occurs at the cladding-solution interface, the surrounding analyte absorbs the transmitted light.

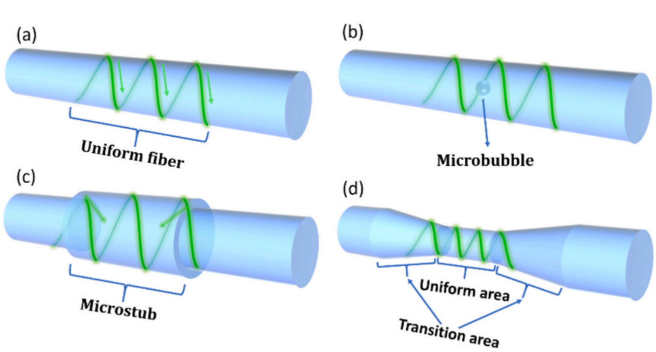

Fig. 2. Concept of the different sensing structures (a) uniform structure; (b) microbubble structure; (c) microstub structure; and (d) tapered structure.

The microbubble structure (Fig. 2b) was created by first cladding-stripping a 3 cm length of sensing fiber. The sensing fiber was cleaved into two sections, and a microcavity with dimensions of approximately 40 μm was micromachined into one end face using a femtosecond laser. Laser micromachining parameters were: linearly polarized laser output, 515 nm wavelength, 290 fs pulse width, 200 kHz repetition rate, 10 μJ pulse energy, 1 mm/s motor speed, 10× microscope objective magnification, and 0.25 NA. After rinsing with alcohol to remove debris, the two end faces were spliced together, resulting in the formation of an inner hollow bubble or more precisely, a microbubble structure.

The microstub structure (Fig. 2c) was fabricated through a delicate sequence of cleaving and splicing. First, a coreless multimode fiber with a 320 μm cladding diameter was coating-stripped and flat cleaved. Second, a coreless multimode fiber with a 400 μm cladding diameter was coating-stripped and flat cleaved. The two bare fiber sections were spliced together and then cleaved to retain a 2 cm length of 400 μm section attached to the 320 μm fiber. Lastly, another 320 μm fiber was prepared and spliced to the free end of the 400 μm section, resulting in a microstub structure with a microstub length of 2 cm and a total sensing length of 3 cm.

The tapered structure (Fig. 2d) was fabricated through flame-assisted tapering of the original fiber. An in-house hydrogen-oxygen flame tapering system was used to fabricate tapered fibers, with setting of uniform region length, uniform region diameter, and transition region length in LabVIEW to obtain the desired taper profile.

Fig. 4 shows the microscope images of the four sensing structures. Fig. 4a shows the uniform structure, with a cladding diameter of 320 μm, and coating diameter of 483 μm. Fig. 4b shows the microbubble structure, with a bubble-like microcavity measuring ~40 μm in each dimension. Fig. 4c showcases the microstub structure comprising 320–400-320 μm cladding diameters. Fig. 4d reveals the uniform waist of the tapered structure, with a cladding diameter of 113 μm.

3. Simulations

Simulations were carried out in the initial stage of experimentation using ZEMAX (Fig. 5) as a feasibility guide to analyze the progression of skew rays within four distinct sensing structures. A comparison was made between the simulated distribution of optical power at the terminal point of the fiber and the distribution obtained through experimental measurements (conducted within an aqueous solution), as shown in Fig. 6. The incident light beam was assumed to possess an angle of 10 deg. upon reaching the input fiber end face. The cladding refractive index is 1.45 which is very close to that of the fiber used and the coating refractive index is 1.37. To accommodate the chosen absorption medium (water), the refractive index was set as 1.33 in order to prevent reflection at the interface.

In the uniform structure (Fig. 7a) the skew rays enter the fiber, undergo total internal reflections, and propagate along a helical path. The rays pass through the sensing region (i.e., the stripped fiber section of 3 cm) and a portion is absorbed by the simulated water environment. By adjusting the incident angle and height continuously, the corresponding power distribution (Fig. 7a) was obtained. The same simulation approach was applied to the other sensing structures as well, such as microbubble structure (Fig. 7b), microstub structure (Fig. 7c), and tapered structure (Fig. 7d), to observe the propagation of light rays and obtain the corresponding power distribution.

For the microbubble structure (Fig. 7b), the light propagates along a spiral path within it. By performing simulations at different incident angles and heights, the corresponding power distribution (Fig. 7b) can be obtained. However, it should be noted that the simulation results may differ significantly from the actual scenario. One possible reason is that in the simulation, the bubble is assumed to be a perfect spherical shape with a vacuum inside. In reality, the fabricated microbubble structure

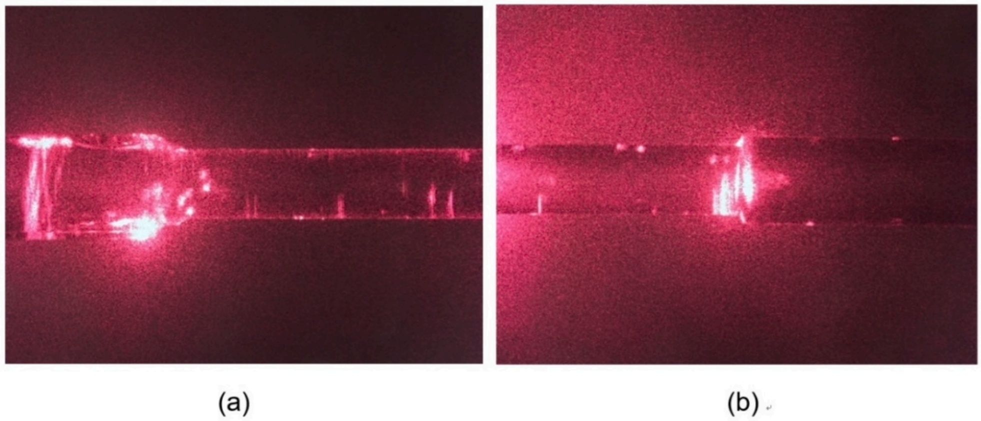

Fig. 3. Microscope images of red-laser illuminated uniform structure, (a) sensing area left interface, and (b) sensing area right interface. (For interpretation of the references to color in this figure legend, the reader is referred to the web version of this article.)

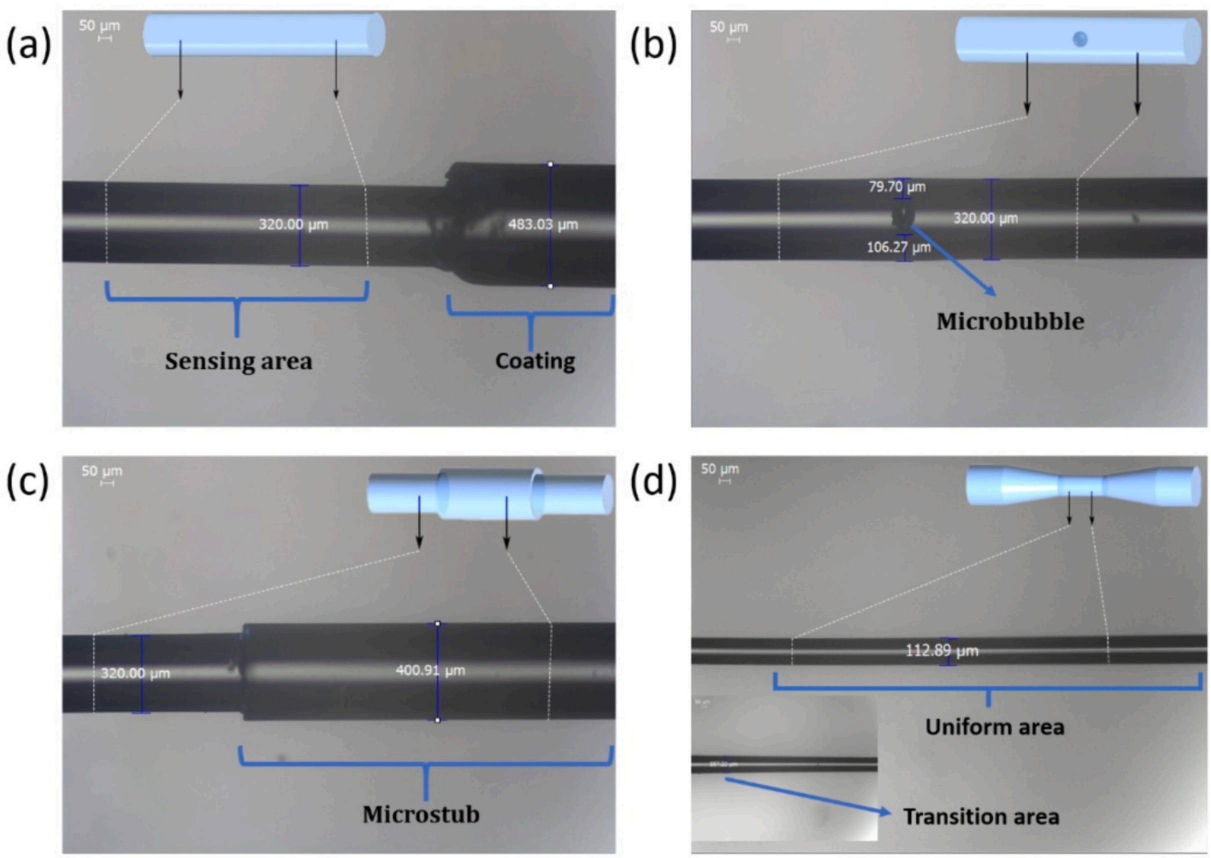

Fig. 4. Microscope images of the different structures based on coreless multimode fiber: (a) uniform structure; (b) microbubble structure; (c) microstub structure; and (d) tapered structure.

approximates a slightly elliptical shape.

These differences would affect the path of light propagation and power distribution, leading to disparities between the simulation results and actual observations. Therefore, in practical applications, besides relying on simulation results, it is necessary to consider the actual fabrication process of the microbubble structure and make appropriate adjustments and optimizations.

The sensing region of the microstub structure (Fig. 7c) has a length of 4 cm, with the microstub itself being 2 cm in length. However, this structure exhibits significant loss during light propagation, mainly due to the diameter-mismatch-induced coupling losses at the two splice points. The simulation results of the microstub structure differ significantly from those of the uniform structure (Fig. 7a). This disparity likely stems from the more complex fabrication process of the microstub structure, involving three cleaving and two splicing steps, and the arc fusion process that can affect the transition shape between two fiber diameters. Consequently, it is crucial to optimize the manufacturing process for the microstub structure to reduce losses and enhance sensing performance.

In the tapered structure (Fig. 7d), the light propagates in a spiral path until the narrow waist region. Due to the reduction in fiber diameter in the narrow waist region, there is an increase in high-order mode loss,

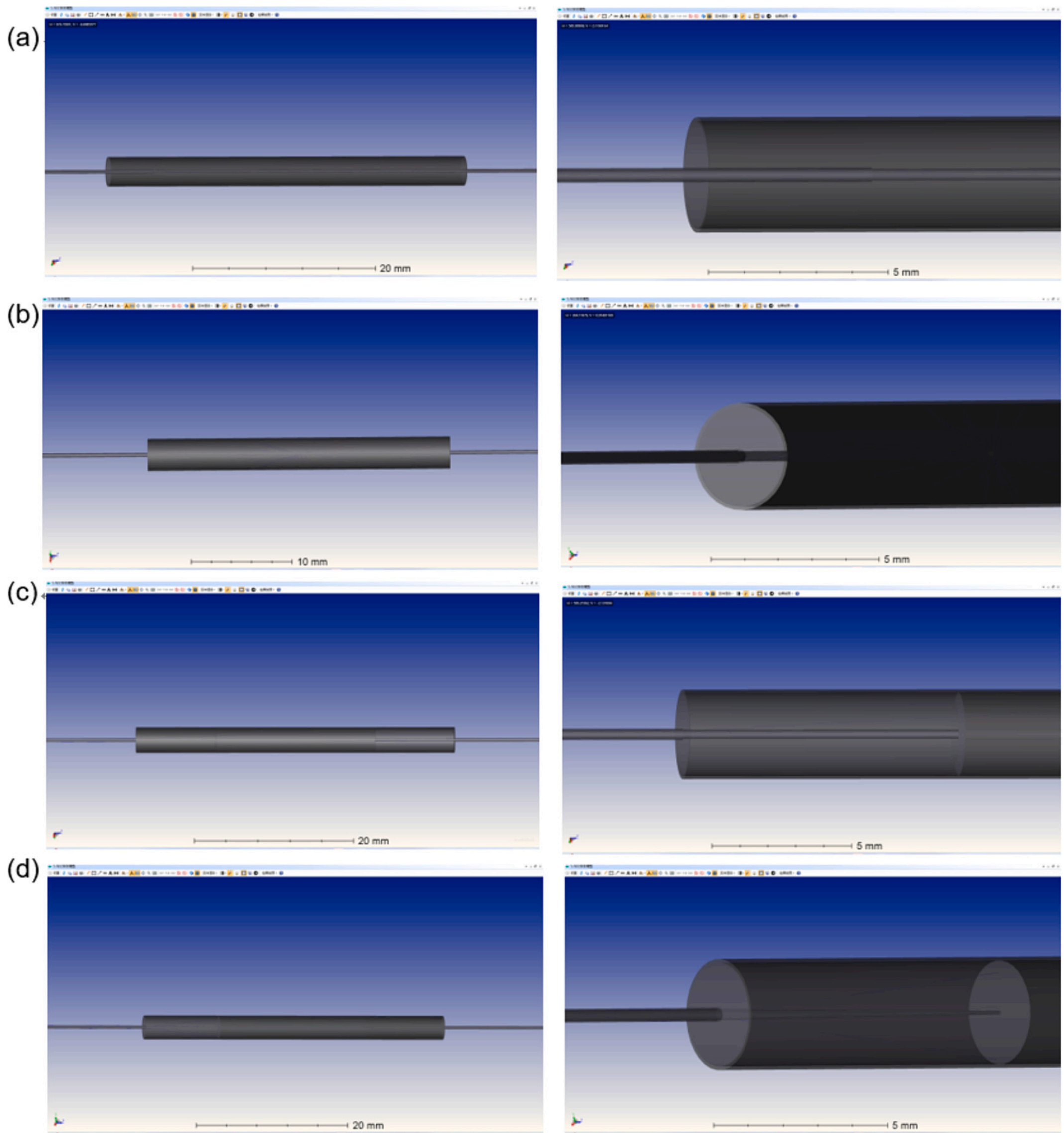

Fig. 5. ZEMAX simulation 3D model of each sensing structure: (a) uniform structure, (b) microbubble structure, (c) microstub structure, and (d) tapered structure.

resulting in significant energy loss. Consequently, compared to the uniform structure, the tapered structure exhibits lower power output at larger angles (Fig. 7d), leading to an overall decrease in power. In the tapered structure, the length of the uniform region is 2 cm, and the transition regions on both sides have lengths of 1 cm each, making the total length of the sensing region 5 cm. The shape variation within the sensing region affects light propagation, leading to increased mode loss in the multimode fiber. Consequently, when designing and implementing tapered structures, the impact of fiber diameter and transition profile on optical transmission needs to be considered. Furthermore, it is possible that the launch angle of light and thus the positions of total internal reflections determine the location of spikes in evanescent field along the fiber taper, which corresponds to the prominent sensing points.

4. Experiments

4.1. Experimental setup

The schematic diagram of the experimental setup for injecting pump light into the sensing fiber is depicted in Fig. 8. The experiment was conducted at varying incident heights and angles, and with a sensing fiber partially immersed in Rhodamine B solution. The sensing fiber is based on coreless multimode fiber made of fused silica with a diameter of 320 μm, a numerical aperture of 0.4, a length of 90 cm, and a bending radius of approximately 40 cm. This sensing fiber was coupled with an unpolarized, single-mode laser source operating at a wavelength of 532 nm. The laser source is very stable (<1% intensity fluctuation) and thus does not require a feedback loop for stabilization. The pump light having a beam diameter of 3.2 mm was collimated using a plano-convex lens with a focal length of 150 mm. A cylindrical plano-convex lens 100 mm scale focal length was utilized to create the light sheet of ~20 μm thickness. However, accurately measuring the thickness of the resulting output ring was challenging due to the skewed angle of the light rays. The flat-cleaved input end of the sensing fiber was affixed to a computer-controlled rotary stage, positioned at the rotational center. By center alignment of the collimated beam at the input end of the sensing fiber using a rotating 3-axis translation stage, the input power and signal-to-noise ratio can be maximized, thereby enhancing the detection sensitivity.

The sensing fiber projected the output light into an integrating-sphere based power meter (Newport 918D-IS-1, 1936-R). A 570 nm long-pass color glass filter was employed to confirm a negligible fluorescence signal, which ensured that the total received optical power was

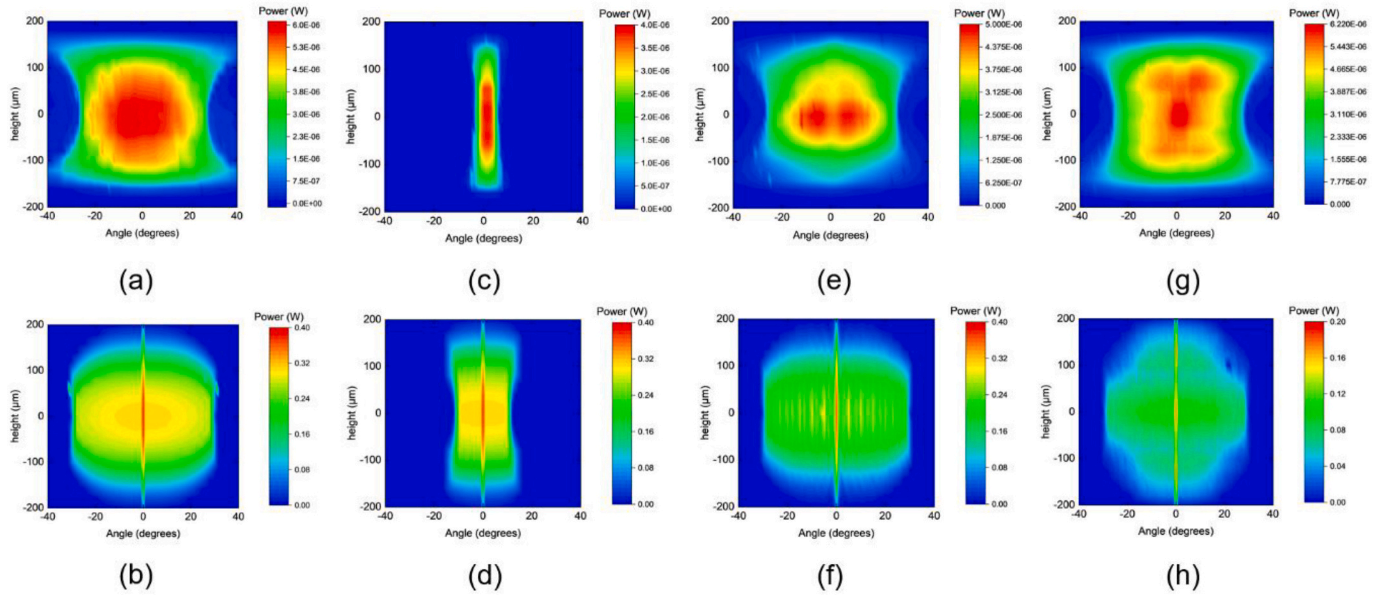

Fig. 6. Comparison of actual and simulated power for each sensing structure: (a) Uniform structure powers characterization. (b) Uniform structure simulated powers. (c) Tapered structure powers characterization. (d) Tapered structure simulated powers. (e) Microstub structure powers characterization. (f) Microstub structure simulated powers. (g) Microbubble structure powers characterization. (h) Microbubble structure simulated powers.

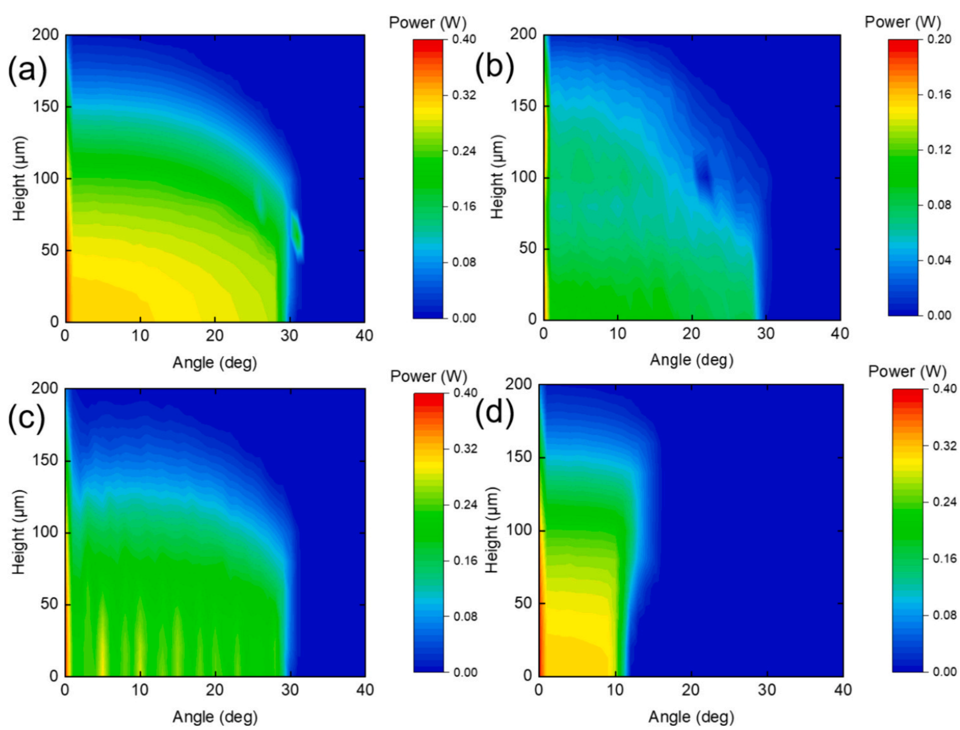

Fig. 7. Simulated output power at various angles and heights for the: (a) uniform structure; (b) microbubble structure; (c) microstub structure; and (d) tapered structure.

composed of the residual pump power. Attenuated measurements were repeated on both the dye solution and pure water (baseline) with the aim of compensating for water absorption losses.

4.2. Experiment results

The testing range covered concentrations spanning from 1 ng/ml to 10^4 ng/ml, with an order of magnitude increase in each concentration level. A total of five discrete concentrations were tested. In the experiments, attenuation is used as a sensing performance metric. The attenuation reflects the responsiveness of the sensor to changes in the analyte concentration. However, if the attenuation is too high, the signal-to-noise ratio becomes poor and consequently the limit of detection worsens. Fig. 9 illustrates the attenuation results for the uniform sensing structure. It is observed that as the concentration increases, the attenuation also increases gradually. Moreover, a localized attenuation is clearly observed in the upper right corner that is characterized by higher positions and larger angles of the light sheet. This indicates

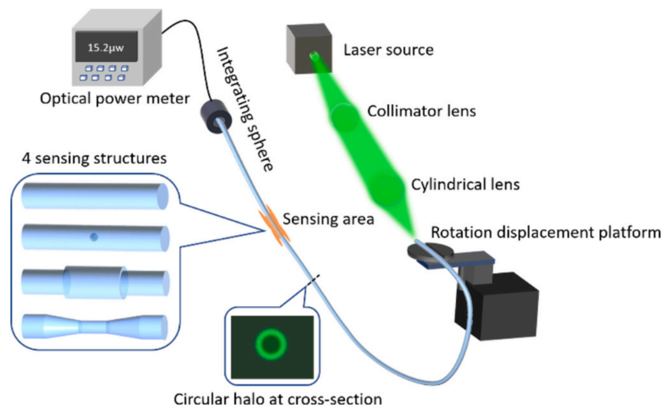

Fig. 8. Experimental setup: laser beam is reshaped into a light sheet before exciting a narrow band of skew rays for maximized sensitivity.

that the absorption effectiveness of the solution is optimal when the light sheet is at the appropriate height and angle within this region. The maximum attenuation peak at the optimal incident height and angle is measured as 6.74 dB.

The absorption-induced attenuation of the microbubble sensing structure was also investigated as depicted in Fig. 10. Similar to that of the uniform structure, the attenuation increases gradually with increasing the concentration. Likewise, a localized attenuation phenomenon is clearly visible in the region of higher light sheet positions and larger incident angles. The maximum attenuation peak for the microbubble structure is measured as 11.38 dB which is slightly higher than the results obtained from the uniform structure.

The attenuation results for the microstub structure (Fig. 11) show similar trend as that of the uniform and microbubble structures. As concentration increases, the attenuation effect gradually intensifies. Additionally, a localized attenuation phenomenon is observed in the region of higher light-sheet positions and larger launch angles, indicating that the optimal height and angle within this region contribute to the best absorption effectiveness of the solution. At the optimal incident height and angle within the microstub structure, the maximum attenuation peak is measured as 9.62 dB, slightly lower than the results obtained with the micro-bubble structure.

For the attenuation results of the tapered structure, on the other hand, significant differences were observed compared to the other three structures (Fig. 12). There is a pronounced localized attenuation in the region of higher light-sheet positions and smaller launch angles. This localized attenuation phenomenon is attributed to the reduction in diameter after the tapering of the optical fiber, which renders the waveguide sensitive to high-order mode cut-off with varying launch conditions. A maximum attenuation peak of 15.03 dB can be achieved within the region of enhanced attenuation by selecting the optimal incident height and angle. These findings indicate that different structures have distinct effects on the attenuation in the design and optimization of fiber-optic sensors. The characteristics of the tapered structure require special attention when selecting the incident position and angle to achieve optimal absorption effectiveness.

Three different heights and launch angles were selected for each sensing structure to investigate the most suitable launch conditions for measuring Rhodamine B (as shown in Fig. 13), taking both sensitivity and linearity into account. Fig. 13a presents the trend of attenuation variations with concentration for three different incident heights and angles in the uniform structure. It is observed that the attenuation is highest with high sensitivity at the position (36°, 180 μm). However, at the position (24°, 160 μm), the attenuation corresponding to a concentration of 10^3 ng/ml is unexpectedly stronger than that of 10^4 ng/ml, which could be attributed to the attenuation peak occurring early in this particular launch condition and photobleaching occurring at higher concentrations. The trend at the position (17°, 160 μm) is similar to that at the position (24°, 160 μm), but the attenuation is weaker for each concentration. This confirms that (36°, 180 μm) is the optimal incident height and angle for the uniform structure. Fig. 13b shows the trend of attenuation variations with concentration for three different incident heights and angles for the microbubble structure. Overall, at the incident angle and height of (38°, 180 μm), the attenuation increases more rapidly with concentration variation, and the final attenuation is also stronger. Therefore, (38°, 180 μm) represents the optimal incident angle and height for sensitivity for the microbubble structure. Fig. 13c

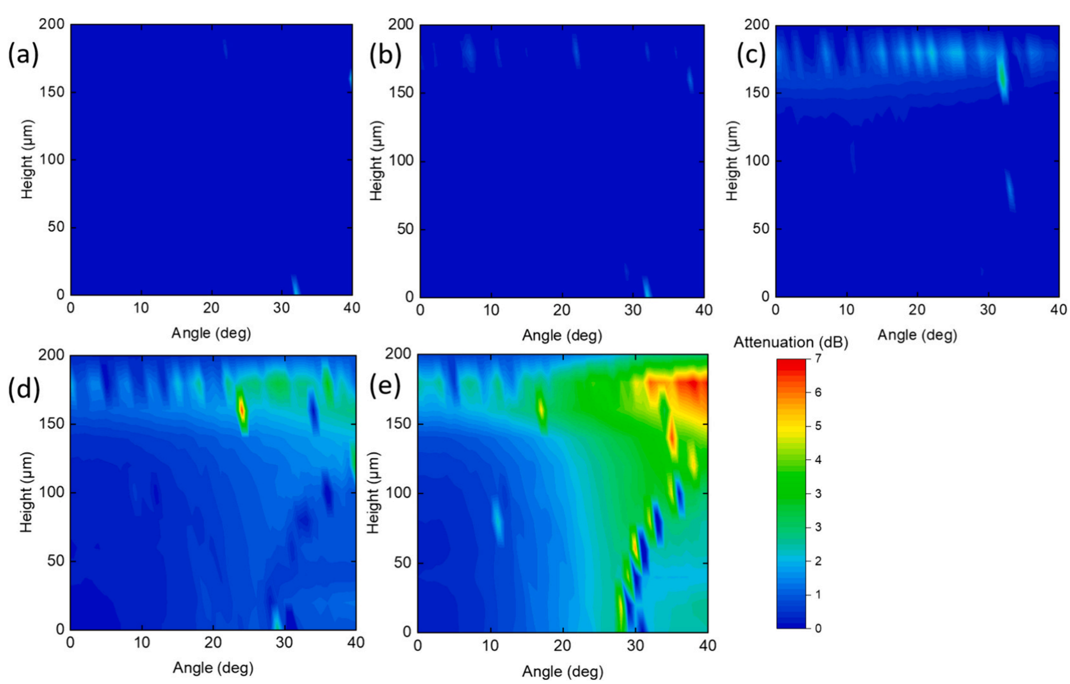

Fig. 9. Absorption-induced attenuation of uniform structure at different concentrations: (a) 1 ng/ml; (b) 10 ng/ml; (c) 100 ng/ml; (d) 1000 ng/ml; and (e) 10,000 ng/ml.

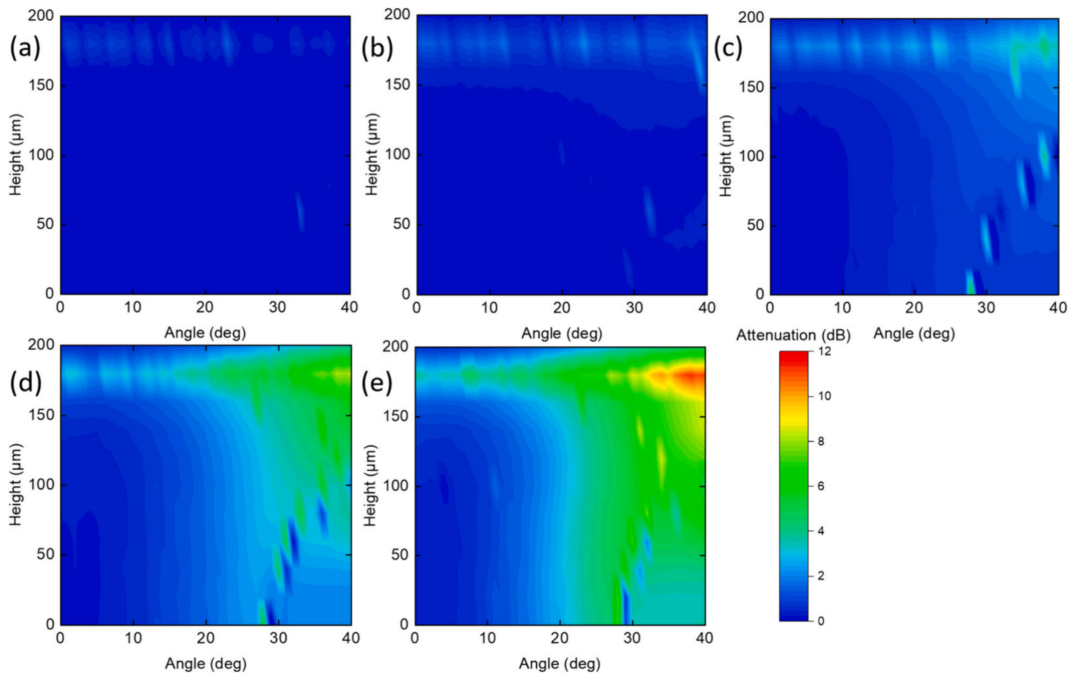

Fig. 10. Absorption-induced attenuation of the microbubble structure at different concentrations: (a) 1 ng/ml; (b) 10 ng/ml; (c) 100 ng/ml; (d) 1000 ng/ml; and (e) 10,000 ng/ml.

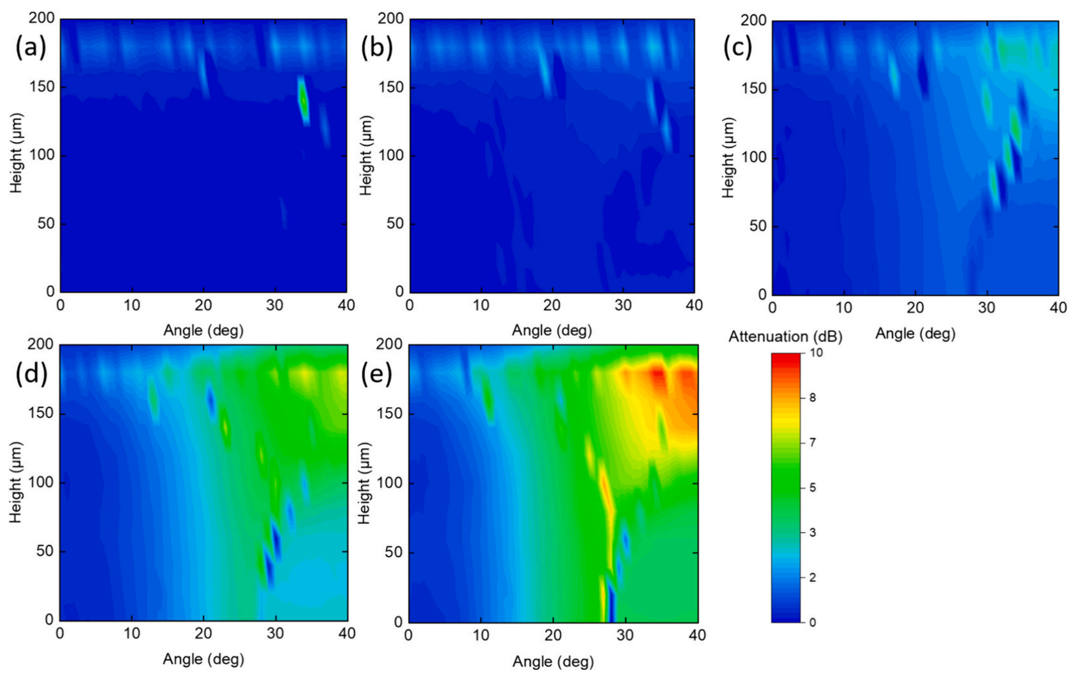

Fig. 11. Absorption-induced attenuation of microstub structure at different concentrations: (a) 1 ng/ml; (b) 10 ng/ml; (c) 100 ng/ml; (d) 1000 ng/ml; and (e) 10,000 ng/ml.

demonstrates the trend of attenuation variations with concentration for three different incident heights and angles for the microstub structure. Comparing the three curves, it is be observed that at the position (35°, 180 μm), the curve of attenuation variation with concentration is the steepest, with the highest slope and the maximum attenuation at the highest concentration. Thus, (35°, 180 μm) represents the optimal incident angle and height for the microstub structure. Fig. 13d displays the trend of attenuation variations with concentration for three different incident heights and angles in the tapered structure. At the position (8°, 160 μm), the attenuation increases roughly linearly with concentration, showing the largest slope and the highest attenuation at the highest concentration. However, at the position (4°, 40 μm), the attenuation variations with concentration are nonlinear and the attenuation is not as high as at the position (8°, 160 μm). At the position (2°, 60 μm), the variations are approximately linear, but with a smaller slope and lower sensitivity. Therefore, (8°, 160 μm) represents the optimal incident angle and height for sensitivity for the tapered structure.

A comparative analysis was conducted between the attenuation of

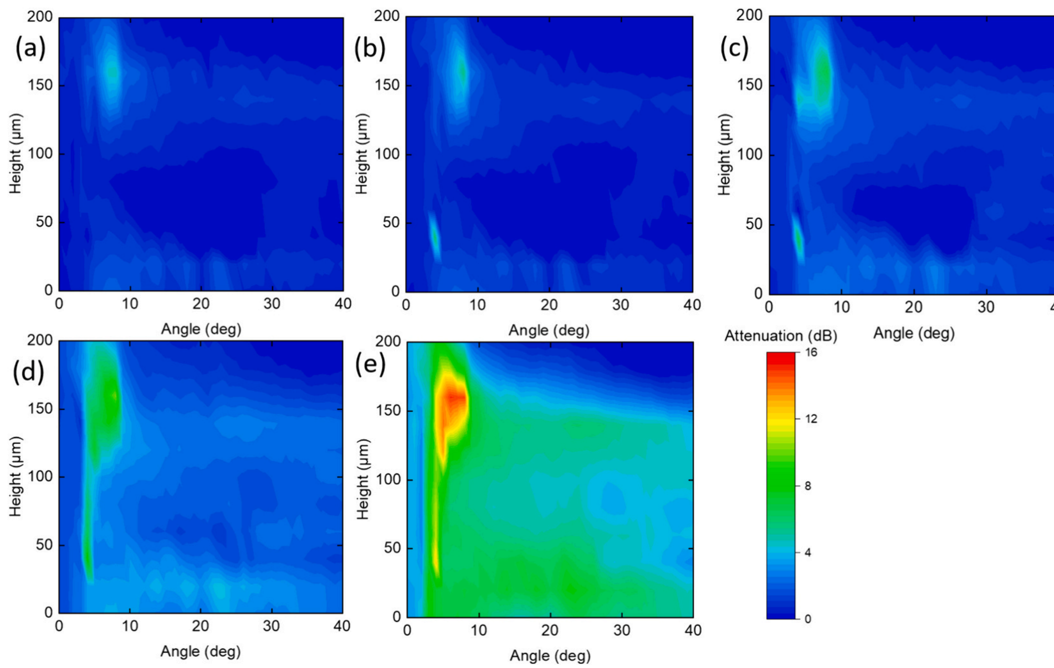

Fig. 12. Absorption-induced attenuation of tapered structure at different concentrations: (a) 1 ng/ml; (b) 10 ng/ml; (c) 100 ng/ml; (d) 1000 ng/ml; and (e) 10,000 ng/ml.

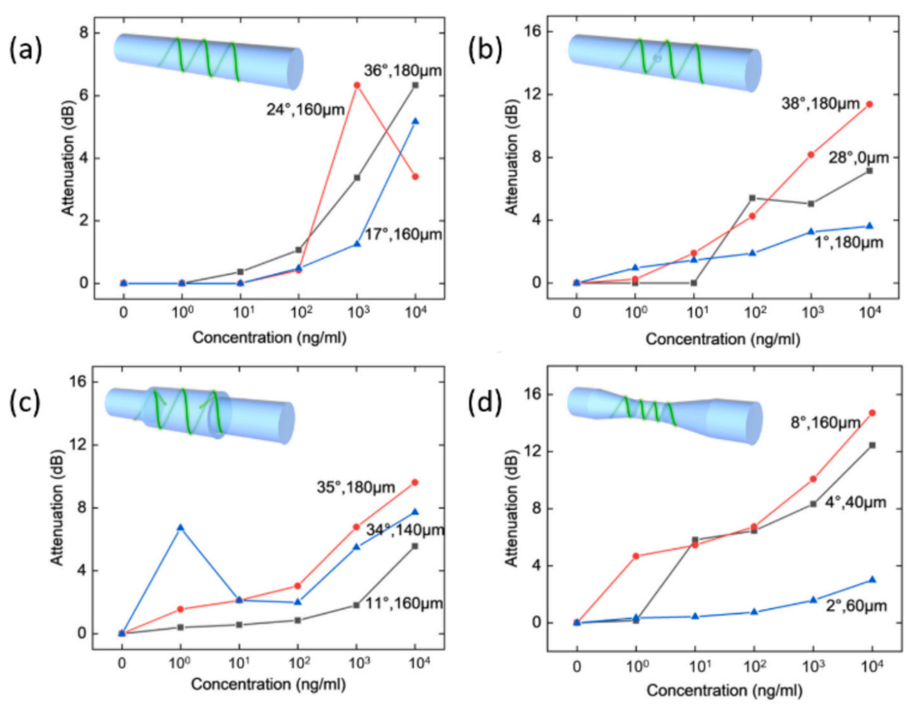

Fig. 13. Changes in absorption-induced attenuation of 4 structures with increasing concentration at 3 different incidence angles and heights: (a) uniform structure; (b) microbubble structure; (c) microstub structure; and (d) tapered structure.

different sensing structures with respect to different concentrations, at their optimal launch conditions (Fig. 14a). From Fig. 14a, it can be observed that the sensing curves for the four structures exhibit a monotonic response, but with different slope gradients that are indicative of the sensitivity. Therefore, it can be concluded that the tapered structure demonstrates the best sensitivity. However, considering that the lengths of the sensing regions differ for the four structures, and the length of the sensing region also affects the sensing performance, for a fair comparison, length normalization is necessary. From Fig. 14b, it can be seen that after length normalization, the microbubble structure exhibits the best sensing performance, achieving a maximum sensitivity of 0.046 (dB/cm) / $dB_{(1\ ng/ml)}$ and a linear-region sensitivity of 0.03953 (dB/cm) / $dB_{(1\ ng/ml)}$ at launch conditions of (38°, 180 μm). This is due to the fact that compared to the tapered structure the hollow microbubble structure not only increases the number of total internal reflections and thus interaction with the analyte, but also induces a week internal Fabry Perot etalon that could increase scattering, which in turn leads to a slightly higher sensitivity.With a measured noise floor

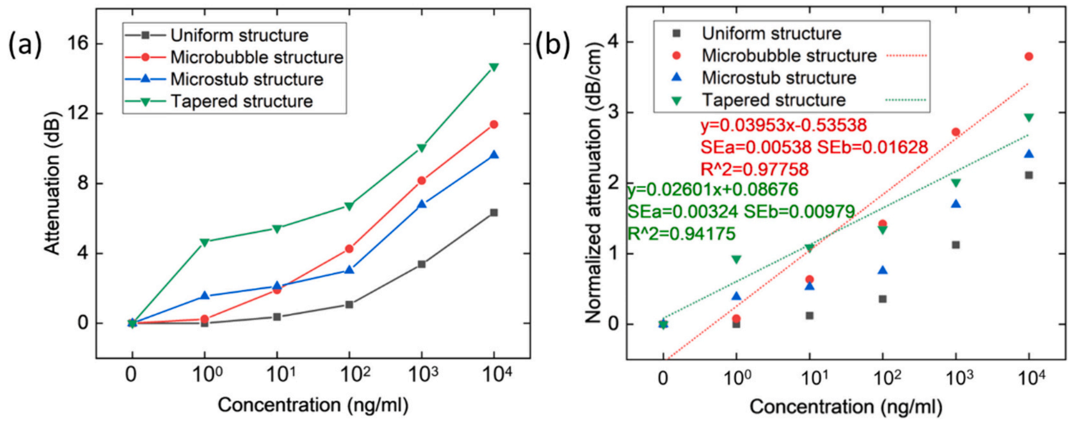

Fig. 14. (a) Variation of absorption-induced attenuation with increasing concentration for each of the four structures at their optimum angle of incidence and height of incidence (Unnormalized); (b) variation of attenuation with increasing concentration for each of the four structures after length normalization at the respective optimum angle of incidence and height of incidence (The x-axis log scale was chosen for ease of viewing; the x-axis dB scale is used for the gradient of the linear fit).

equivalent to 0.0276 dB, the std. of noise is 0.00994 dB, the limit of detection (LoD) is 0.236 $dB_{(1\ ng/ml)}$ or 1.028 ng/ml with 3.03 cm sensing length. In addition, one possible way to improve the linearity of the results could be to restrict the dynamic range of the sensor (range of concentrations).

To assess the repeatability of the sensors, a series of attenuation experiments were performed, wherein concentration tests were carried out for the tapered structure. We chose the taper design for repeatability over the microbubble structure due to the better reproducibility. The microbubble fabrication process often yields hollow bubbles of different shapes and dimensions, which is not suitable for practical application where the production yield needs to be sufficiently high. We performed three consecutive tests on the conical structure over a period of 18 h to obtain the mean and standard deviation of the three data sets under the same launch conditions, subsequent to these trials, an evaluation of the associated errors was undertaken with the findings depicted in Fig. 15. A maximum error of 1.29 dB was observed, which suggests a reasonably consistent sensing performance.

The resistance to temperature fluctuations of fiber-optic sensors is extremely critical, as temperature fluctuations can affect the accuracy and reliability of the sensor. A length of uniform coreless multimode fiber,[32] being the least-sensitive design, naturally has good resistance to temperature fluctuations, due to the lack of interference or mode coupling effects. The tapered coreless multimode fiber should not be sensitive in our case due to its relatively large waist diameter (relative to wavelength of light), and thus weak evanescent field overlap with the environment.[9] Murugan, G. et al. used a microstub fiber design[33] to create a micro-laser and measured its emission wavelength using an optical spectrum analyzer. If the microstub was temperature sensitive, the relatively slow wavelength sweep measurement would not have been possible, which infers a low temperature cross-sensitivity as well. For the microbubble structure design (nominated best design), the temperature cross-sensitivity was investigate, as shown in Fig. 16. A temperature control box was installed surrounding the sensing region without direct contact with the sensing fiber. The sensing region was heated from 25 °C to 50 °C, measured with a thermocouple at the fiber location. The change in optical power was recorded with a total of 600 data points, with one data point every 1 s. Experimentally, it was demonstrated that the microbubble structure exhibits good resistance to temperature fluctuations. The temperature resistance was judged by observing the change in the received optical power between temperature steps. The first step is room temperature around 25.5 °C, sustained for 0–2 min, then heating started in the second minute, with the sensing area warmed up for 2–5 min, and was maintained at around 50.5 °C for 5–10 min. No obvious changes in the optical power (and thus attenuation) were observed during the temperature test, indicating good thermal resistance.

As an evanescent-wave-based chemical sensor, the objective was to identify the most effective design for chemical sensing. In the previous

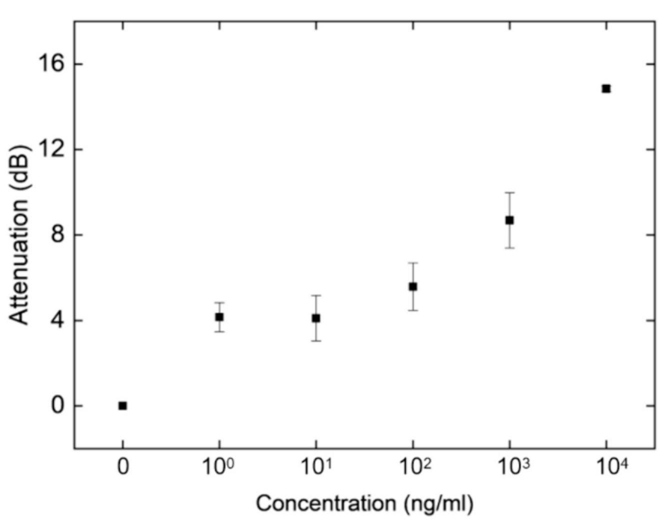

Fig. 15. Repeatability data at different RhB concentrations for the tapered structure.

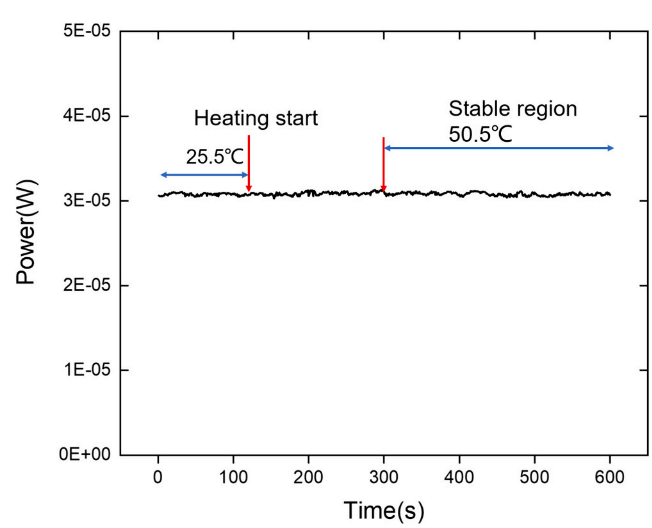

Fig. 16. Temperature influence test of the microbubble sensing structure.

trial runs, it was observed that the tapered structure displayed the most significant attenuation in signal strength, measuring at 15.03 dB, when immersed in a Rhodamine B solution of 10 μg/ml concentration. Nevertheless, the variability in the length of the sensing region during the fabrication process could potentially influence sensing performance, necessitating the need to standardize attenuation measurements. Through the tapering process, the effective length of the sensing region was expanded to 5 cm, leading to a normalized signal reduction of 3.01 dB/cm. Conversely, the uniform structure exhibited a sensing region length of 3 cm, with the most substantial signal attenuation reaching 6.74 dB and a normalized attenuation of 2.25 dB/cm. Similarly, the microbubble structure also maintained a 3 cm sensing region, yielding a maximum signal attenuation of 11.38 dB and a normalized attenuation of 3.79 dB/cm. Additionally, the microstub structure featured a 4 cm sensing region, demonstrating a peak signal attenuation of 9.62 dB and a normalized attenuation of 2.40 dB/cm. The outcomes derived from these assessments indicate that the microbubble structure stands out in terms of sensing performance after sensing length normalization with a maximum sensitivity of 0.046 (dB/cm) / $dB_{(1\ ng/ml)}$ and a linear-region sensitivity of 0.03953 (dB/cm) / $dB_{(1\ ng/ml)}$ at launch conditions of (38°, 180 μm). The microbubble design improves sensitivity by four orders of magnitude compared to previous work, which focused on uniform fiber and comparing the sensitivity improvement between light-sheet generated skew rays and other types of light incidence.[32] It's uniform exterior surface and robustness makes it particularly suitable for repeated chemical measurements.

5. Conclusions

In conclusion, the aim of this study was to create a chemical sensor head with high sensitivity yet robust. To achieve this, four distinct sensing structures were examined, all relying on coreless multimode fiber (320 μm core diameter, sensing region length of 30–50 mm) were studied through simulation and experiment verification: uniform, microbubble, microstub, and tapered. Each sensing structure was separately interrogated with beam-shaped skew rays through a light-sheet injection method. The outcomes of the experiments revealed that the microbubble configuration showcased the highest normalized sensitivity to Rhodamine B, registering at 0.046 (dB/cm) / $dB_{(1\ ng/ml)}$, corresponding to an LoD of 1.028 ng/ml with a sensing length of 3 cm. The results show that the microbubble structure improves the sensitivity by four orders of magnitude compared to previous work. It is worth noting that potential avenues for refining the microbubble structure's sensitivity and detection limit include modifications to microbubble size and dimensions, surface adjustments of gold nanoparticles, and the utilization of fluorescence spectroscopy for detection. In essence, this study effectively demonstrates the exceptional sensing capabilities of the coreless multimode fiber structure, boasting remarkable sensitivity, resistance to temperature fluctuations, and overall robustness.

CRediT authorship contribution statement

Lukui Xu: Methodology, Writing – original draft. **Tingting Zhuang:** Investigation, Visualization. **Bonan Liu:** Methodology. **Jinyu Wang:** Methodology, Writing – review & editing. **Mamoona Khalid:** Methodology, Writing – review & editing. **Soroush Shahnia:** Methodology, Writing – review & editing. **Christophe A. Codemard:** Methodology, Writing – review & editing. **Zhiyong Bai:** Methodology, Writing – review & editing. **Shen Liu:** Methodology. **George Y. Chen:** Conceptualization, Funding acquisition, Methodology, Supervision, Writing – review & editing. **Yiping Wang:** Supervision, Writing – review & editing.

Declaration of competing interest

The authors declare no conflicts of interest.

Data availability

Data will be made available on request.

Acknowledgements

This work was supported by the National Natural Science Foundation of China (Grant Number: 62275172, 62005138); Natural Science Foundation of Guangdong Province (2023A1515012893); Guangdong Provincial Department of Science and Technology (2022A1515010183); Shenzhen Science and Technology Program (Grant Number: KQTD20221101093605019); Science, Technology and Innovation Commission of Shenzhen Municipality (Grant Number: JCYJ20220818095615034); research start-up fund for high-end talent at Shenzhen University.

References

[1] Food Safety. https://www.who.int/news-room/fact-sheets/detail/food-safety, 2022.
[2] S. Olenik, H.S. Lee, F. Güder, The future of near-field communication-based wireless sensing, Nat. Rev. Mater. 6 (2021) 286–288.
[3] Paul Chevalier, Marco Piccardo, Guy-Maël de Naurois, Ilan Gabay, Abraham Katzir, Federico Capasso, In-water fiber-optic evanescent wave sensing with quantum cascade lasers, Sensors Actuators B Chem. 262 (2018) 195–199. ISSN 0925–4005.
[4] N.S. Fabián, A.B. Socorro-Leránoz, I.D. Villar, S. Díaz, I.R. Matías, Multimode-Coreless-Multimode Fiber-Based Sensors: Theoretical and Experimental Study, J. Lightwave Technol. 37 (15) (2019) 3844–3850.
[5] Donato Luna-Moreno, David Monzon-Hernándeź, Joel Villatoro, et al., Optical fiber hydrogen sensor based on core diameter mismatch and annealed Pd–Au thin films, Sensors Actuators B Chem. 125 (1) (2007) 66–71. JUL, https://doi.org/10.1016/j.snb.2007.01.036.
[6] Takuya Okazaki, Tomoaki Watanabe, Hideki Kuramitz, Evanescent-wave Fiber optic sensing of the anionic dye Uranine based on ion association extraction, Sensors 20 (10) (2020), https://doi.org/10.3390/s20102796. MAY.
[7] Yunkun Wang, Bing Tan, Shurong Liu, et al., An optical fiber-waveguide-fiber platform for ppt level evanescent field-based sensing, Sensors Actuators B Chem. 306 (2020), https://doi.org/10.1016/j.snb.2019.127548. MAR.
[8] Arijit Datta, Appasani Mahendra Babu, Ardhendu Saha, Enhanced sensitivity of fiber optic evanescent wave absorption-based concentration sensor by shining a Bessel–Gauss beam and effect of fiber bending on the sensor response: a theoretical analysis, Opt. Eng. 58 (5) (2019), https://doi.org/10.1117/1.OE.58.5.056112. MAY.
[9] Nor Akmar Mohd Yahya, Mohd Rashid Yusof Hamid, Siti Azlida Ibrahim, et al., H_2 sensor based on tapered optical fiber coated with MnO_2 nanostructures, Sensors Actuators B Chem. 246 (2017) 421–427. JUL, https://doi.org/10.1016/j.snb.2017.02.084.
[10] Chunlan Liu, Lingling Li, Rui Wang, et al., Fiber microsphere SPR sensor and its detection of low concentration Hg^{2+}, Opt. Fiber Technol. 64 (2021) https://doi.org/10.1016/j.yofte.2021.102534. JUL.
[11] D. Paul, S. Dutta, D. Saha, et al., LSPR based ultra-sensitive low cost U-bent optical fiber for volatile liquid sensing, Sensors Actuators B Chem. 250 (2017) 198–207. OCT, https://doi.org/10.1016/j.snb.2017.04.171.
[12] Sandra Börner, Rozalia Orghici, Siegfried R. Waldvogel, et al., Evanescent field sensors and the implementation of waveguiding nanostructures, Appl. Opt. 48 (4) (Feb. 2009) B183–B189, https://doi.org/10.1364/AO.48.00B183.
[13] Y. Wu, B.C. Yao, A.Q. Zhang, et al., Graphene-based D-shaped fiber multicore mode interferometer for chemical gas sensing, Opt. Lett. 39 (20) (Oct. 2014) 6030–6033, https://doi.org/10.1364/AO.48.00B183.
[14] Xuegang Li, Ning Chen, Xue Zhou, et al., In-situ DNA detection with an interferometric-type optical sensor based on tapered exposed core microstructured optical fiber, Sensors Actuators B Chem. 351 (Jan. 2022), https://doi.org/10.1016/j.snb.2021.130942.
[15] E. Schartner, G. Tsiminis, M. Henderson, S. Warren-Smith, T. Monro, Quantification of the fluorescence sensing performance of microstructured optical fibers compared to multi-mode fiber tips, Opt. Express 24 (2016) 18541–18550.
[16] Springer, Boston, MA. Fluorescence Sensing. In: Lakowicz, J.R. (eds) Principles of Fluorescence Spectroscopy. doi: https://doi.org/10.1007/978-0-387-46312-4_19 (2006).
[17] Lanhua Liu, Didi Shan, Xiaohong Zhou, Hanchang Shi, Baodong Song, Floris Falke, Arne Leinse, René Heideman, TriPleX™ waveguide-based fluorescence biosensor for multichannel environmental contaminants detection, Biosens. Bioelectron. 106 (2018) 117–121. ISSN 0956–5663.
[18] R.A. Lieberman, L.L. Blyler, L.G. Cohen, A distributed fiber optic sensor based on cladding fluorescence, J. Lightwave Technol. 8 (2) (1990) 212–220.
[19] S. Otto, Wolfbeis. Fluorescence optical sensors in analytical chemistry, TrAC Trends Anal. Chem. 4 (7) (1985) 184–188. ISSN 0165–9936.
[20] K. Muto, Electric-discharge sensor utilizing fluorescent optical fiber, J. Lightwave Technol. 7 (7) (1989) 1029–1032.

[21] Gang Ding Peng, Zhengjun Xiong, P.L. Chu, Fluorescence decay and recovery in organic dye-doped polymer optical fibers, J. Lightwave Technol. 16 (12) (1998) 2365–2372.
[22] Yu Ruoyu Wang, Xiaohong Zhou Xiang, Lan-hua Liu, Hanchang Shi, A reusable aptamer-based evanescent wave all-fiber biosensor for highly sensitive detection of Ochratoxin. A, Biosens. Bioelectron. 66 (2015) 11–18. ISSN 0956-5663.
[23] V.P.N. Venkataraj, P. Radhakrishnan Nampoori, M. Kailasnath, Chemically tapered multimode optical Fiber probe for fluoride detection based on fluorescence quenching of curcumin, IEEE Sensors J. 15 (10) (2015) 5584–5591.
[24] J. Ma, W. Bock, Dramatic performance enhancement of evanescent-wave multimode fiber fluorometer using non-Lambertian light diffuser, Opt. Express 15 (2007) 16457–16470.
[25] G.Y. Chen, C.A. Codemard, P.M. Gorman, J.S. Chan, M.N. Zervas, Angle-Resolved Characterization and Ray-Optics Modeling of Fiber-Optic Sensors, J. Lightwave Technol. 33 (24) (2015) 5210–5217.
[26] G. Herskowitz, H. Kobrinski, U. Levy, Optical power distribution in multimode fibers with angular-dependent mode coupling, J. Lightwave Technol. 1 (4) (1983) 548–554.
[27] Daniel Feuermann, Jeffrey M. Gordon, Mahmoud Huleihil, Light leakage in optical fibers: experimental results, modeling and the consequences for solar concentrators, Sol. Energy 72 (3) (2002) 195–204. ISSN 0038-092X.
[28] R. Venkataraj, V.P.N. Nampoori, P. Radhakrishnan, M. Kailasnath, Chemically Tapered Multimode Optical Fiber Probe for Fluoride Detection Based on Fluorescence Quenching of Curcumin, IEEE Sensors J. 15 (10) (2015) 5584–5591.
[29] Jinyu Wang, George Y. Chen, Wu Xuan, Xu Haolan, Tanya M. Monro, Tongyu Liu, David G. Lancaster, Light-sheet skew ray-enhanced localized surface Plasmon resonance-based chemical sensing, ACS Sens. 5 (1) (2020) 127–132.
[30] A. Snyder, D.J. Mitchell, Leaky rays on circular optical fibers, J. Opt. Soc. Am. 64 (1974) 599.
[31] G.Y. Chen, S. Shahnia, T.M. Monro, D.G. Lancaster, Force Sensors Using the Skew-Ray-Probed Plastic Optical Fibers, IEEE Photon. J. 10 (3) (2018) 1–8, 6802208.
[32] G.Y. Chen, et al., Light-Sheet Skew-Ray Enhanced Pump-Absorption for Sensing, J. Lightwave Technol. 37 (9) (2019) 2140–2146.
[33] G. Murugan, S. Bakhtiari-Gorajoobi, C. Codemard, M. Mohd Nasir, G. Chen, et al., Optical microstub resonator lasers, Proc. SPIE 8960, Laser Resonators, Microresonators Beam Control XVI. ISSN: 0277-786X 896018 (2014), https://doi.org/10.1117/12.2039672.

Dr. George Y. Chen graduated with a 4-year MEng (Bachelor's and Master's joint degree) from Imperial College London in 2009, in the field of electronics and electrical engineering with computer science. He completed his PhD from the Optoelectronics Research Centre at the University of Southampton in 2013. He worked in an industrial research lab as a postdoctoral research fellow for SPI Lasers Ltd. from 2013 to 2015. He joined the University of South Australia as a research fellow in 2015, and played a critical role in establishing the Laser Physics and Photonic Devices Laboratories and a Joint Research Lab between the University of South Australia and Shandong Academy of Sciences. He was a part of the MinEx CRC. He joined Shenzhen University as a Professor in 2021, with a focus on the research of long-range distributed vibration sensing technologies. He currently serves as the deputy director of the Shenzhen Key Laboratory of Ultrafast Laser Micro-Nano Manufacturing Science and Technology. He is a co-inventor of 1 PCT patent, and he has co-authored a book chapter published by CRC Press. He has published 36 journal papers as first/corresponding author, with 11 invited talks. He has led and participated in various projects, with a total funding of $3.6M AUD and 46.6M RMB. He has been on the technical program committee of one of the largest conferences in his field (OFS) between 2018–2021. He has created and hosted a workshop in Asia's largest photonics conference (APC). He is an editorial board member of Scientific Reports (Nature), a guest editor of Sensors (MDPI), and Optica / IEEE Senior Member.

Dr. Yiping Wang is a distinguished professor, doctoral supervisor, National Outstanding Youth, 10,000-Person Leader, Optica Fellow, director of the "Key Laboratory of Optoelectronic Devices and Systems of Ministry of Education", and director of the "Guangdong and Hong Kong Joint Research Centre for Optical Fibre Sensors" at the School of Physics and Optoelectronic Engineering, Shenzhen University. In 2003, he received a PhD degree in Optical Engineering from Chongqing University, and worked in the research area of optical fiber sensing and applications at Shanghai Jiaotong University (postdoctoral fellow), Hong Kong Polytechnic University (postdoctoral fellow), Jena Photonics Technology Research Institute in Germany (Humboldt scholar), and Southampton University in the UK (Curie scholar). In 2012, he was appointed distinguished professor at Shenzhen University and established the Fiber-Optic Sensing Innovation Team, "Guangdong and Hong Kong Joint Research Centre for Optical Fibre Sensors", "Shenzhen Key Laboratory of Photonic Devices and Sensing Systems for Internet of Things", and "Shenzhen Optical Materials Femtosecond Laser Preparation Technology Engineering Laboratory". His research team consists of 92 members, including 20 full-time researchers (4 national level talents and 12 teachers), 10 postdoctoral students, 19 doctoral students, and 43 Master's degree students. Prof. Wang has been researching fiber optical sensing technologies and applications for several decades, with main directions including: (1) Preparation technology of fiber-optic sensor components; (2) Fiber-optic sensing technology for extreme environments; (3) Fiber-optic sensing technology for life and health. He received the First and Second Prizes of the Natural Science Award of the Ministry of Education, first prize of the Shenzhen Natural Science Award, First Prize of the Sichuan Science and Technology Progress Award, First Prize of the Guangdong Optical Society Optical Science and Technology Award, National Excellent Doctoral Dissertation Award, the European Union Marie Curie International Talent Introduction Fund Award, German Humboldt Research Fund Award, and Shenzhen May 1st Labor Medal. He has hosted 32 national key research and R&D plans, JKW XX engineering special projects, and national natural science key projects. He has published 420 SCI papers (with over 10,000 SCI citations and an h-index of 50), and 16 papers with over 100 SCI citations each; 120 authorized patents (25 foreign patents); Ranked as a Chinese highly cited scholar and in the Top 2% of global scientists with lifelong scientific influence. He is also an Editorial board member of Applied Optics and Photonic Sensors, and the Vice Chairman of the Guangdong Optical Society.